Editors' Suggestion | Featured in Physics

Spectral Universality of Elastoinertial Turbulence

Sami Yamani,[1,*] Bavand Keshavarz,[1] Yashasvi Raj,[1] Tamer A. Zaki,[2]
Gareth H. McKinley,[1] and Irmgard Bischofberger[1,†]
[1]Department of Mechanical Engineering, Massachusetts Institute of Technology, Cambridge, Massachusetts 02139, USA
[2]Department of Mechanical Engineering, Johns Hopkins University, Baltimore, Maryland 21218, USA

(Received 28 January 2021; accepted 25 May 2021; published 9 August 2021)

Dissolving small amounts of polymer into a Newtonian fluid can dramatically change the dynamics of transitional and turbulent flows. We investigate the spatiotemporal dynamics of a submerged jet of dilute polymer solution entering a quiescent bath of Newtonian fluid. High-speed digital Schlieren imaging is used to quantify the evolution of Lagrangian features in the jet revealing a rich sequence of transitional and turbulent states. At high levels of viscoelasticity, we identify a new distinct transitional pathway to elastoinertial turbulence (EIT) that does not feature the conventional turbulent bursts and instead proceeds via a shear-layer instability that produces elongated filaments of polymer due to the nonlinear effects of viscoelasticity. Even though the pathways to the EIT state can be different, and within EIT the spatial details of the turbulent structures vary systematically with polymer microstructure and concentration, there is a universality in the power-law spectral decay of EIT with frequency, f^{-3}, independent of fluid rheology and flow parameters.

DOI: 10.1103/PhysRevLett.127.074501

The loss of stability in inertially dominated flows of dilute polymer solutions (typically $\lesssim$100 ppm) results in a turbulent state known as elastoinertial turbulence (EIT) with distinctly different structural features compared to Newtonian turbulence (NT) or elastic turbulence [1]. While the onset of NT is characterized by intermittent turbulent bursts, or "puffs," between extended laminar regions, these puffs disappear when the polymer concentration increases and, as the authors note, a "different type of disordered motion" sets in [1], which is not well understood. We show that at high levels of viscoelasticity, i.e., high elasticity numbers, this distinct inertio-elastic state provides a new pathway to EIT in a submerged fluid jet.

Recent experiments and simulations [2–5] in planar channel flow show that increasing the polymer concentration results in a transition to turbulence at a lower Reynolds number than for a Newtonian fluid due to the existence of unstable wall modes [6] and center modes [7]. Following the transition to EIT, the growth of near-wall vortical structures in the channel is predominantly in the spanwise direction, as opposed to NT where vortical structures grow in both the spanwise and streamwise directions [1,2]. Moreover, EIT displays intermittent "hibernating" turbulent states, i.e., long-lived recurrent transient dynamical modes that are distinctly different to NT [8] and have recently been shown to be instability waves [9–11]. Characteristic dynamical features of EIT include weaker vortices, streamwise streaks, and a reduction in the average total shear stress at the wall, even as the normal stress differences in the flow increase [12]. In addition to changes in the shape of the vortical structures in the flow, the spectral characteristics of the instantaneous velocity profile also change significantly when viscoelasticity is present [13,14] and important discrepancies exist between different reported values for the exponent characterizing the power-law decay of the energy spectrum [15], making quantitative measurements of the velocity field necessary [16].

A limited number of studies have considered the structure of EIT in jets or other spatially developing flows. Early experimental work using laser Doppler velocimetry showed that viscoelasticity suppresses the smaller scale eddies in a submerged jet [17]. Recently, direct numerical simulations of viscoelastic planar jets have shown that the viscous dissipation rate in a turbulent polymeric jet is strongly attenuated, with a significant portion of the turbulent energy flux being stored elastically in the stretched polymer chains and subsequently returned to the flow [18]. This energy storage changes the turbulent structures leading to a reduction in the spreading of the jet, i.e., making the jet narrower, as the Weissenberg number (Wi) increases.

Despite these recent theoretical advances in understanding EIT, there is a lack of quantitative experimental work studying the associated flow structures. We are aware of only one particle image velocimetry (PIV) study for the specific case of grid turbulence in a channel, which investigated the power-law exponent characterizing the decay in the spectrum of velocity fluctuations in a dilute polymer solution at a fixed Reynolds number and polymer molecular weight [19]. A more recent PIV study documented the unique process of "relaminarization" that is possible in complex viscoelastic flows [20]. For a certain

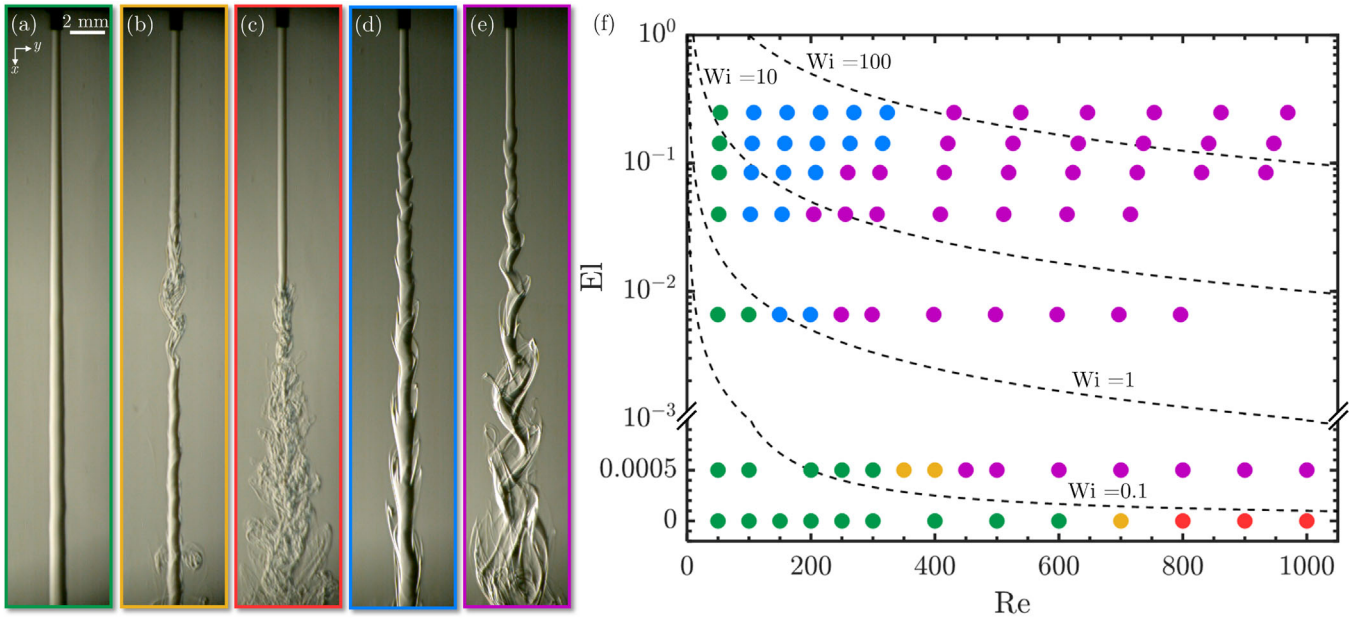

FIG. 1. Flow transitions in a submerged jet. (a)–(e) Laminar (green circle), turbulent bursts (yellow circle), NT (red circle), EIF (blue circle), and EIT (violet circle) state. (f) State diagram for $L_{\max} = 91.4$, i.e., PEO with $M_w = 8 \times 10^6$ g/mol. To represent the Newtonian jet on this state diagram, we use a linear ordinate for El $\leq 10^{-3}$.

range of Reynolds and Weissenberg numbers, the interaction between fluid inertia and polymer stresses is strong enough to eliminate Newtonian-like turbulence, but is too weak to trigger EIT, thus enabling access to a new stable state. However, the combination of the relatively weak vortical structures in EIT (as compared to NT) and the inherent difficulties of PIV measurements close to rigid walls of tubes and channels have prevented direct observation of the spanwise vortical structures predicted by numerical simulations [21].

Inspired by early qualitative imaging of viscoelastic turbulence [22,23], we use high-speed Schlieren imaging to reveal the local fluctuating concentration field in either a submerged Newtonian or viscoelastic jet. Unlike PIV, Schlieren imaging does not require addition of particles as flow tracers, and reveals the boundaries of the fine-scale material elements along the refractive index gradient in a Lagrangian manner as they are convected through the domain. See the Supplemental Material [24] for details on our Schlieren imaging system, which includes Ref. [25]. We study the transition to turbulence and the resulting spatiotemporal dynamics of an unforced submerged jet of dilute polymer solution entering a quiescent bath of its Newtonian solvent. We identify a distinct transitional pathway to EIT, which eliminates the turbulent bursts observed in the transition to NT. Instead, a convective shear layer instability produces locally elongated filaments of viscoelastic material, which we term elastoinertial filaments (EIF). Remarkably, even though the pathways to EIT and the spatial features of EIT vary with changes in fluid properties including polymer molecular weight and concentration, the temporal features of the unsteady jet far from the nozzle are universal and characterized by a power-law frequency decay that is markedly different from the spectrum of Newtonian turbulence.

In our experiments, a submerged jet of dilute aqueous polyethylene oxide (PEO) solution enters a bath of water [Fig. 1]. To systematically vary the viscoelasticity, we use a range of polymer molecular weights, M_w, and concentrations, c. The rheological characterization and properties of the solutions discussed in this Letter are summarized in Sec. III and Table S1 provided in the Supplemental Material and includes Refs. [26–31]. All of the solutions are dilute with $c/c^* < 1$, where c^* is the coil overlap concentration. To attain the required refractive index gradient for Schlieren imaging, 1% wt. sucrose is added to all solutions. The addition of sucrose changes the viscosity by ~1% and does not affect the elasticity of the solutions. The relevant dimensionless numbers characterizing the jet are (i) the Reynolds number $\mathrm{Re} = \rho U(2R)/\eta_0$, where ρ is the fluid density, U is the mean flow velocity at the nozzle, $R = 257$ μm is the radius of the jet at the nozzle exit, and η_0 is the zero shear-rate viscosity of the dilute solution, (ii) the elasticity number $\mathrm{El} = \eta_p \lambda/\rho R^2$, where η_s and $\eta_p = \eta_0 - \eta_s$ are, respectively, the solvent and polymer contribution to the total viscosity in the limit of zero shear rate, and λ is the extensional relaxation time, and (iii) the polymer chain extensibility $L_{\max} = r_{\max}/\langle r_0^2 \rangle^{1/2}$, where $r_{\max} \sim M_w$ is the length of a fully extended polymer chain, $\langle r_0^2 \rangle^{1/2} \sim M_w^{\nu}$ is the equilibrium root-mean-square end-to-end separation of the polymer in the coil state, and ν is the solvent quality parameter [32].

A summary of the distinct dynamical states observed in our jet injection experiments is shown in Figs. 1(a)–1(e) and Movie S1. At a low Reynolds number, the jet is laminar and stable [Fig. 1(a)]. As the Reynolds number increases, a transition to turbulence can happen via two distinctly different pathways, namely (i) through the transient growth and decay of turbulent bursts for the Newtonian jet and viscoelastic jets with low El and $L_{\max}$ [Fig. 1(b)] and (ii) through the development and growth of EIF for viscoelastic jets with high El and $L_{\max}$ [Fig. 1(d)]. The EIF state appears to be a fundamentally different pathway to turbulence, which eliminates the axially localized turbulent bursts, or "puffs," and replaces them with elongated filaments of highly stretched, polymer rich fluid around the core of the jet. The dynamics of turbulent bursts and EIF states are compared side by side in Movie S2.

We construct a state diagram summarizing these different dynamical states of the jetting flow from the three independent dimensionless numbers that characterize the fluid rheology (El, $L_{\max}$) and the flow (Re), respectively, and show a cross sectional slice of this three-dimensional state diagram in Fig. 1(f) for $L_{\max} = 91.4$ (see Fig. S2 of the Supplemental Material for a three-dimensional representation). Contours of constant Weissenberg number are hyperbolae, where $\mathrm{Wi} = \mathrm{El} \cdot \mathrm{Re} = 2(\eta_p/\eta_0)(U\lambda/R) = 2(1-\beta)(U\lambda/R)$ and $\beta = \eta_s/\eta_0$. The NT and EIT states are distinguished based on the value of the power-law decay exponent in the spectral density of concentration fluctuations, as discussed in Fig. 3.

Increasing fluid elasticity in the range of moderate Weissenberg numbers, when elastic, viscous, and inertial effects are all important ($0 < \mathrm{Wi} \lesssim 10$, $\mathrm{El} < 0.05$), has a destabilizing effect resulting in a transition to turbulence at markedly lower Reynolds numbers ($\mathrm{Re} = 400$) compared to the Newtonian jet ($\mathrm{Re} = 800$) [Fig. 1(f)]. This destabilizing behavior has been observed in bounded flows [1], and predicted by linear perturbation theory for both free shear and bounded flows [3,33]. Our state diagram provides the first quantitative mapping of this phenomenon in a spatially developing flow such as a jet undergoing nonlinear breakdown to turbulence.

However, further increases in elasticity, such that viscous effects can be ignored compared to elastic and inertial effects ($\mathrm{Wi} \gtrsim 10$, $\mathrm{El} > 0.05$), restabilizes the jet and the turbulent bursts are replaced with highly elongated filaments (denoted EIF). This stabilization of the jet creates a reentrant region on the state diagram that is characterized by Weissenberg numbers of order unity [Fig. 1(f)] and shifts the transition to turbulence to higher Reynolds numbers. Recognizing that the importance of viscous and elastic effects compared to inertial effects are characterized by Re^{-1} and El, respectively, it is clear that in this region inertial and elastic effects dominate and viscous effects can be ignored.

Our work identifies the EIF state as a distinct viscoelastic transition and a new pathway to turbulence, in which elastic tensile stresses first suppress the turbulent bursts and then lead to a shear layer instability. The jet can be viewed as an "elastic" fluid column that slowly decelerates through momentum diffusion as it enters the quiescent tank. The combination of elasticity and deceleration of the fluid column results in a buckling-type instability that breaks the axisymmetry of the high-speed jet. The shear layer at the boundary of the jet grows with distance from the nozzle and leads to the development of the EIF structures. In these highly elongated filaments of fluid that surround the core of the jet, viscoelastic tensile stresses increase substantially. Each filament experiences a combination of unsteady shear and extension. When the resulting normal stress differences are high compared to the shear stress in the jet, we may expect the strong stretching of the polymer chains along the streamlines to eliminate turbulent bursts. Using the finitely extensible nonlinear elastic dumbbell model we know that $\eta_e \approx 2\eta_p L_{\max}^2$ is the steady extensional viscosity of the fully stretched chains [34]. Based on our experiments with a wide range of polymer molecular weights (or $L_{\max}$) and polymer concentrations [$\sim(1-\beta)$], we find an appropriate criterion for the elimination of turbulent bursts and the development of EIF to be $\eta_e/\eta_0 \sim (1-\beta)L_{\max}^2 \sim \mathcal{O}(100)$.

The turbulent bursts and EIF resulting from the shear layer instability observed in Fig. 1 are both transitional pathways that ultimately lead to EIT. In this turbulent state the jets can exhibit significantly different spatial features at a given El and Re as a result of the differing extensibilities of the polymer chains leading to different levels of tensile stresses in the fluid, as shown in Fig. 2. To quantitatively compare the spatial features of EIT, we recognize that mixing processes in these inertio-elastic turbulent flows are the result of progressive stretching and folding into intermingled material elements and, ultimately, molecular diffusion of the polymer into the surrounding solvent [35]. For the short timescales of interest here, the effect of intermolecular diffusion is negligible because the Péclet number $\mathrm{Pe} = RU/D \gg 1$; the diffusion coefficient of the polymer in its solvent is very small and scales as $D \sim M_w^{-\nu}$ [32]. We can thus define a time-averaged two-point correlation coefficient, $\bar{\xi}(y^*)$, for lateral displacements of size Δy calculated from a series of Schlieren images of the spatial concentration fluctuations, where $y^* = \Delta y/R$ (see Sec. V of the Supplemental Material [24]). We use the scale of segregation $S = \int_0^\infty \bar{\xi} dy^*$ to characterize the mean size of the intermingled and deformed material elements observed in the turbulent jet [35]. As we show in Fig. 2(c), for a series of jets at a fixed elasticity number and Reynolds number, the scale of segregation (suitably adjusted for a finite integration width and constant background intensity; cf. Sec. V of the Supplemental Material [24]) increases monotonically with M_w, and hence $L_{\max}^2$. An analysis of the finitely extensible nonlinear elastic dumbbell model at high Wi (see the Supplemental Material [24]) shows that this scaling is consistent with

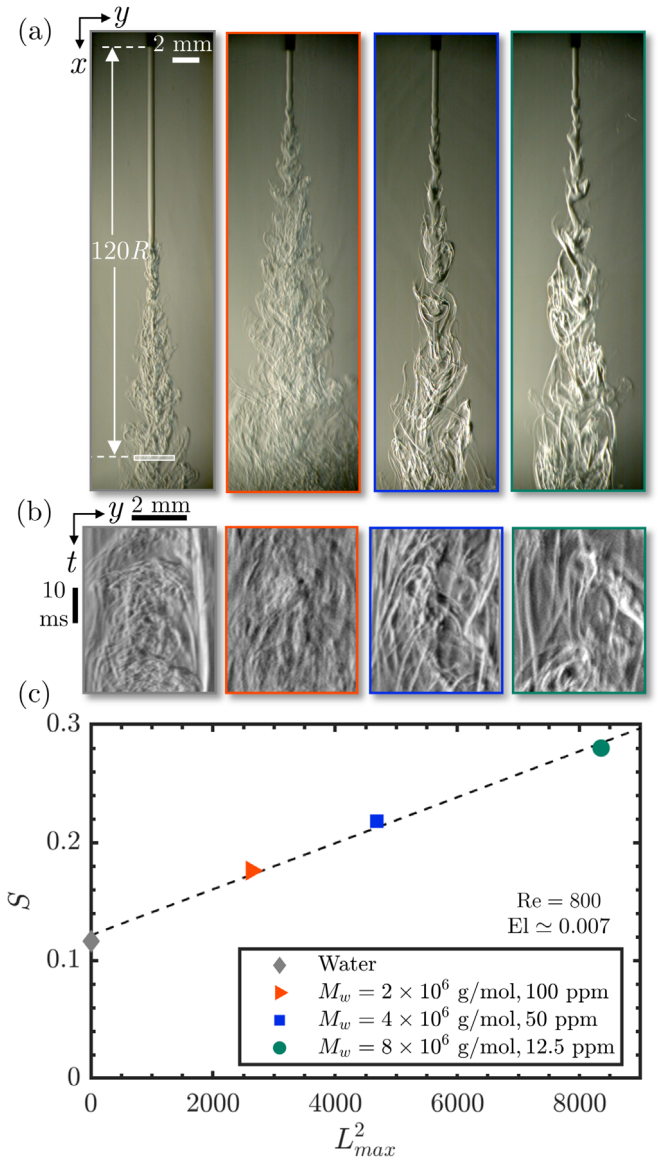

FIG. 2. (a) From left to right: snapshots of a Newtonian (water) jet and PEO solution jets with $M_w = 2 \times 10^6$ g/mol, $c = 100$ ppm, $M_w = 4 \times 10^6$ g/mol, $c = 50$ ppm, and $M_w = 8 \times 10^6$ g/mol, $c = 12.5$ ppm, respectively. (b) Kymographs of the concentration fluctuations at the Eulerian cross section at a distance $120R$ from the nozzle, shown with a white rectangle. (c) Evolution of the scale of segregation S with polymer extensibility $L^2_{\max}$. The error bars from repeated measurements of S are smaller than the symbol size.

the expectation that the ratio of the first normal-stress difference to shear stress also depends on the maximum extensibility, $L^2_{\max}$.

Finally, we quantify the temporal features of EIT. Remarkably, fluid elasticity challenges even our most strongly held notions of turbulence, specifically the $-5/3$ decay rate of its energy spectra [36]. We evaluate the temporal power spectral density $P(f)$, where f is the frequency of the concentration fluctuations in jets, in the EIT state for a wide range of Re, El, and $L_{\max}$ at the centerline of the jet, as shown in Fig. 3. At $\mathrm{Re} = 400$, where a Newtonian jet is still laminar, all jets in the EIT state, regardless of their transitional pathway or spatial features, exhibit a spectral decay of $P(f) \sim f^{-3}$ at high frequencies. Given the large values of the Péclet number in these high M_w polymer jets, the effects of diffusivity are negligibly small. Therefore, the power-law scaling of concentration fluctuations is equivalent to probing the turbulent energy spectrum in the inertial range [37] and it is clear that the classical cascade of turbulent energy is dramatically altered by the polymer. With frequency nondimensionalized by the Zimm relaxation time, λ_{Zimm}, the f^{-3} decay starts at $\lambda_{\mathrm{Zimm}} f \sim 1$, illustrating that the macromolecular solute starts to have an impact on the turbulent flow at frequencies on the order of the polymer relaxation rate, which depends on the polymer molecular weight $\lambda_{\mathrm{Zimm}} \sim M_w^{3\nu}$. In the dilute limit, the Zimm relaxation time is independent of the concentration [32] and all data series obtained from the same molecular weight polymers superpose. However, normalization with the Zimm relaxation time fails to superpose the data series obtained from polymer solutions with different molecular weights.

At a higher Reynolds number, $\mathrm{Re} = 800$, both Newtonian and viscoelastic jets are turbulent [Fig. 3(b)]. The classical scaling of Newtonian turbulence [37,38] is verified after the Newtonian jet transitions to turbulence at $\mathrm{Re} = 800$, with $P(f) \sim f^{-5/3}$ in the "inertio-convective" range [37]. The dashed line denotes the characteristic frequency at the onset of the power-law decay, calculated based on the Kolmogorov timescale [39]. For the viscoelastic jets, the onset frequency is lower and the f^{-3} slope is observed for all investigated El and $L_{\max}$, suggesting a temporal universality for the EIT state observed in dilute polymer solutions under good solvent conditions [32]. Indeed, we use the scaling $P(f) \sim f^{-3}$ as our criterion for identifying the EIT jet states in the state diagram shown in Fig. 1 and in the Supplemental Material [24].

The abscissa of Fig. 3(b) is nondimensionalized by the characteristic strain rate in the jet at the nozzle, $\dot{\varepsilon} \sim U/R$. Using the strain rate for nondimensionalization superposes all data series independent of Re, El, and $L_{\max}$ (see also Fig. S5 of the Supplemental Material [24], where we show 14 datasets at different Reynolds numbers). The data collapse highlights a universality that was hypothesized by E.J. Hinch [40], and which we demonstrate is robust beyond the case of isotropic turbulence [14,19,41]: the polymer chains sustain a persistent time-averaged rate of strain $\langle \dot{\varepsilon} \rangle$ through their continuous extension and relaxation. Dimensional arguments require that this constant strain rate (with dimensions of $[\mathrm{time}]^{-1}$) scales with the spectral density of the turbulent energy per unit mass at a particular wave number k (which has dimensions of $[\mathrm{length}^3/\mathrm{time}^2]$) according to $\langle \dot{\varepsilon} \rangle \sim [E(k)k^3]^{0.5}$, and therefore in elastically dominated turbulence we can anticipate

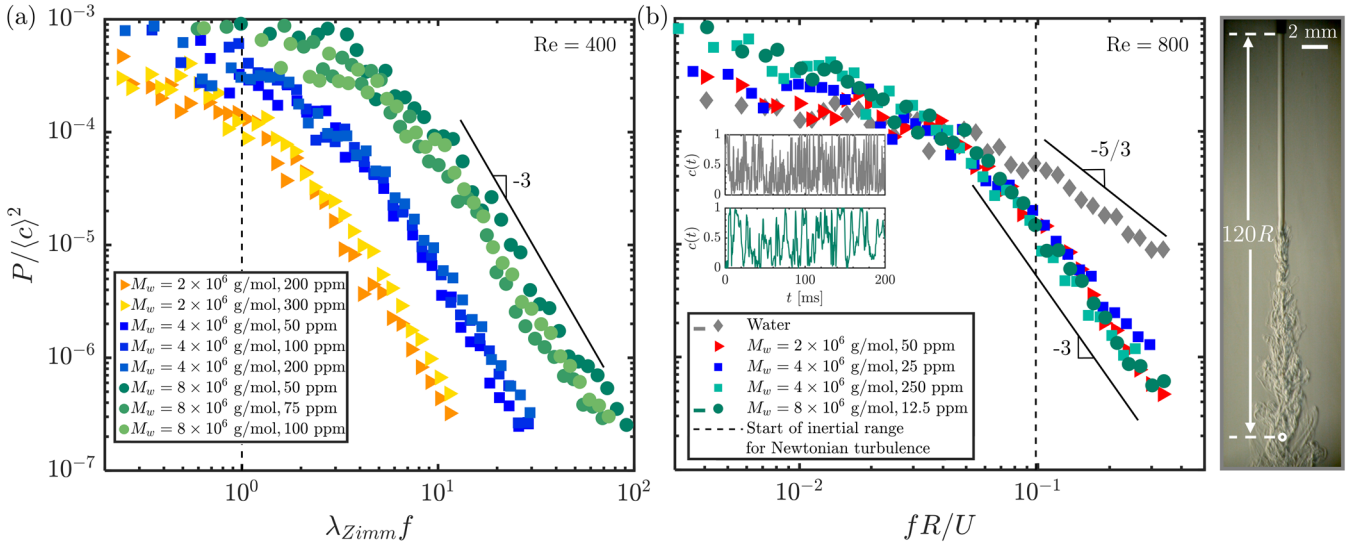

FIG. 3. (a) Frequency spectra of the fluctuations in the local concentration in turbulent polymer jets at Re = 400 and for a vertical distance 120R from the nozzle at the centerline of the jet. The abscissa and ordinate are nondimensionalized with the Zimm relaxation time, λ_{Zimm}, and the square of the mean local concentration, $\langle c \rangle^2$, respectively. The dashed line denotes $\lambda_{\mathrm{Zimm}} f = 1$. The corresponding Newtonian jet is stable at this condition. (b) Temporal power spectral density for concentration fluctuations at Re = 800 for the Newtonian jet and polymer solutions with different molecular weights and concentrations. The abscissa is nondimensionalized with the strain rate at the exit of the nozzle, U/R. The dashed line denotes the start of the inertial range for Newtonian turbulence. The data acquisition point is shown with a hollow circle in the image shown on the right. The insets in (b) compare the raw time signal of concentration fluctuations for the Newtonian jet and for a jet of PEO solution ($M_w = 8 \times 10^6$ g/mol, $c = 12.5$ ppm).

that $E(k) \sim k^{-3}$ [19,40]. In the convectively dominated flows studied here [37], where Taylor's frozen flow hypothesis holds due to the small concentration fluctuations (see the Supplemental Material, which includes Refs. [42–45]), the power-law decay rate of the frequency spectrum for concentration fluctuations is a surrogate for the decay rate of the wave number spectrum for turbulent energy. This power-law scaling provides comprehensive evidence for the universality observed for all concentrations and molecular weights studied.

Our results chart the rich landscape of the turbulent fluid dynamics of dilute polymer solutions. Despite the often-cited calming effect of polymers on turbulence, when viscous and elastic effects interplay (Wi $\lesssim 10$) the effects of increasing fluid elasticity (El) are initially destabilizing. At higher Wi, and in the presence of fluid inertia, the normal stress differences arising from nonlinear elasticity recover their celebrated stabilizing influence [33,46,47]. Using Schlieren imaging, which enables quantitative visualization of the turbulent dynamics of dilute polymer solutions, we have elucidated two routes to EIT; one mediated by turbulent bursts and the other through EIF. Which path is followed depends on the elasticity of the fluid and the extensibility of the dissolved macromolecule. The resulting EIT state that develops in the submerged jet far from the nozzle is different from Newtonian turbulence: the coherence of the large scales is more pronounced and turbulent dispersion is appreciably hindered. The striking qualitative changes in the Schlieren images are matched by a persistent and unambiguous change in the spectral decay rate from the "$-5/3$ power law" expected from Newtonian turbulence to a -3 rate of decay for the elastoinertial regime of jet turbulence. Despite the inconsistencies noted in previously reported power laws for EIT [15], the f^{-3} power law observed in our work is an invariant quantitative measure that can be used as a first step to connect the drag reduction empirically observed in viscoelastic turbulent flows and the time-varying inertio-elastic structures that characterize such processes.

We are grateful to Dr. James W. Bales for his advice and support on building the Schlieren imaging setup. We acknowledge the support of the Natural Sciences and Engineering Research Council of Canada (NSERC), [CGSD2-532512-2019]. Cette recherche a été financée par le Conseil de recherches en sciences naturelles et en génie du Canada (CRSNG), [CGSD2-532512-2019]. This work was also supported in part by the National Science Foundation (NSF) Grant No. CBET-2027870 to MIT and CBET-2027875 to JHU.

*Corresponding author.
syamani@mit.edu
†Corresponding author.
irmgard@mit.edu

[1] D. Samanta, Y. Dubief, M. Holzner, C. Schäfer, A. N. Morozov, C. Wagner, and B. Hof, Proc. Natl. Acad. Sci. U.S.A. **110**, 10557 (2013).

[2] A. Roy, A. Morozov, W. van Saarloos, and R. G. Larson, Phys. Rev. Lett. **97**, 234501 (2006).
[3] P. Garg, I. Chaudhary, M. Khalid, V. Shankar, and G. Subramanian, Phys. Rev. Lett. **121**, 024502 (2018).
[4] I. Chaudhary, P. Garg, G. Subramanian, and V. Shankar, J. Fluid Mech. **908**, A11 (2021).
[5] J. Page, Y. Dubief, and R. R. Kerswell, Phys. Rev. Lett. **125**, 154501 (2020).
[6] I. Chaudhary, P. Garg, V. Shankar, and G. Subramanian, J. Fluid Mech. **881**, 119 (2019).
[7] M. Khalid, I. Chaudhary, P. Garg, V. Shankar, and G. Subramanian, J. Fluid Mech. **915**, A43 (2021).
[8] M. D. Graham, Phys. Fluids **26**, 101301 (2014).
[9] S. J. Lee and T. A. Zaki, J. Fluid Mech. **820**, 232 (2017).
[10] A. Shekar, R. M. McMullen, S.-N. Wang, B. J. McKeon, and M. D. Graham, Phys. Rev. Lett. **122**, 124503 (2019).
[11] A. Shekar, R. M. McMullen, B. J. McKeon, and M. D. Graham, J. Fluid Mech. **897**, A3 (2020).
[12] L. Xi and M. D. Graham, Phys. Rev. Lett. **104**, 218301 (2010).
[13] Y. Dubief, V. E. Terrapon, and J. Soria, Phys. Fluids **25**, 110817 (2013).
[14] P. C. Valente, C. B. da Silva, and F. T. Pinho, Phys. Fluids **28**, 075108 (2016).
[15] V. Steinberg, Phys. Rev. Lett. **123**, 234501 (2019).
[16] V. Steinberg, Annu. Rev. Fluid Mech. **53**, 27 (2021).
[17] N. S. Berman and H. Tan, AIChE J. **31**, 208 (1985).
[18] M. C. Guimarães, N. Pimentel, F. T. Pinho, and C. B. da Silva, J. Fluid Mech. **899**, 208 (2020).
[19] R. Vonlanthen and P. A. Monkewitz, J. Fluid Mech. **730**, 76 (2013).
[20] G. H. Choueiri, J. M. Lopez, and B. Hof, Phys. Rev. Lett. **120**, 124501 (2018).
[21] J. M. Lopez, G. H. Choueiri, and B. Hof, J. Fluid Mech. **874**, 699 (2019).
[22] M. Hibberd, M. Kwade, and R. Scharf, in *Progress and Trends in Rheology* (Springer, New York, 1982), pp. 228–232.
[23] S. Riediger, in *Drag Reduction in Fluid Flows*, edited by R. H. J. Sellin and R. J. Moses (1989), p. 303.
[24] See the Supplemental Material at http://link.aps.org/supplemental/10.1103/PhysRevLett.127.074501 for details on Schlieren imaging setup, sample preparation, rheological characterization, and data analysis methods.
[25] G. S. Settles, *Schlieren and Shadowgraph Techniques* (Springer, New York, 2001).
[26] R. Pamies, J. G. H. Cifre, M. d. C. L. Martínez, and J. G. de la Torre, Colloid Polym. Sci. **286**, 1223 (2008).
[27] A. Rajappan and G. H. McKinley, Sci. Rep. **9**, 18263 (2019).
[28] L. E. Rodd, T. P. Scott, J. J. Cooper-White, and G. H. McKinley, Applied Rheology **15**, 12 (2005).
[29] N. Burshtein, K. Zografos, A. Q. Shen, R. J. Poole, and S. J. Haward, Phys. Rev. X **7**, 041039 (2017).
[30] K. Devanand and J. C. Selser, Macromolecules **24**, 5943 (1991).
[31] V. Tirtaatmadja, G. H. McKinley, and J. J. Cooper-White, Phys. Fluids **18**, 043101 (2006).
[32] M. Rubinstein and R. H. Colby, *Polymer Physics* (Oxford University Press, New York, 2003).
[33] P. K. Ray and T. A. Zaki, Phys. Fluids **26**, 014103 (2014).
[34] R. B. Bird, R. C. Armstrong, and O. Hassager, *Dynamics of Polymeric Liquids. Vol. 1: Fluid Mechanics* (Wiley, New York, 1987).
[35] P. V. Danckwerts, Appl. Sci. Res. **3**, 279 (1952).
[36] J. L. Lumley, *Stochastic Tools in Turbulence* (Courier Corporation, New York, 2007).
[37] S. Corrsin, J. Appl. Phys. **22**, 469 (1951).
[38] G. I. Taylor, Proc. R. Soc. A **164**, 476 (1938).
[39] A. N. Kolmogorov, in *Dokl. Akad. Nauk SSSR*, Vol. 30 (1941), pp. 301–305.
[40] E. J. Hinch, Phys. Fluids **20**, S22 (1977).
[41] A. Fouxon and V. Lebedev, Phys. Fluids **15**, 2060 (2003).
[42] J. L. Lumley, Phys. Fluids **8**, 1056 (1965).
[43] G. Heskestad, J. Appl. Mech. **32**, 735 (1965).
[44] G. He, G. Jin, and Y. Yang, Annu. Rev. Fluid Mech. **49**, 51 (2017).
[45] A. M. Oboukhov, Isv. Geogr. Geophys. Ser. **13**, 58 (1949).
[46] J. M. Rallison and E. J. Hinch, J. Fluid Mech. **288**, 311 (1995).
[47] P. K. Ray and T. A. Zaki, Phys. Fluids **27**, 014110 (2015).